Analytical transmission electron microscopy at organic interfaces

Angela E. Goode*[1], Alexandra E. Porter[1], Michał M. Kłosowski[1], Mary P. Ryan[1], Sandrine Heutz[1], David W. McComb*[2]

1. Department of Materials and London Centre for Nanotechnology, Imperial College London, Exhibition Road, London, SW7 2AZ, UK

2. Department of Materials Science and Engineering and Center for Electron Microscopy and Analysis, Ohio State University, 1305 Kinnear Road, Columbus, OH 43212.

*aeg08@ic.ac.uk, mccomb.29@osu.edu

Abstract

Organic materials are ubiquitous in all aspects of our daily lives. Increasingly there is a need to understand interactions between different organic phases, or between organic and inorganic materials (hybrid interfaces), in order to gain fundamental knowledge about the origin of their structural and functional properties. In order to understand the complex structure-property-processing relationships in (and between) these materials, we need tools that combine high chemical sensitivity with high spatial resolution to allow detailed interfacial characterisation. Analytical transmission electron microscopy (TEM) is a powerful and versatile technique that can fulfil both criteria. However, the application of analytical TEM to organic systems presents some unique challenges, such as low contrast between phases, and electron beam sensitivity. In this review recent analytical TEM approaches to the nanoscale characterisation of two systems will be discussed: the hybrid collagen/mineral interface in bone, and the all-organic donor/acceptor interface in OPV devices.

1. Introduction

Recent instrumental advances in the transmission electron microscope (TEM) include aberration correctors for improved electron optics, as well as monochromators [1] which reduce the energy spread of the electron beam. These allow the formation of smaller (sub-angstrom) electron probes, and the resolution of finer (>100 meV) energy features in electron energy-loss spectra (EELS), respectively. It is now possible to acquire chemical signals from atomic columns [2, 3] or even single atoms [4, 5] in certain favourable, mainly *inorganic,* samples. These recent analytical benefits have been slow to translate to organic systems. In fact, it could be argued that the use of brighter, smaller electron probes actually makes electron-beam induced damage more common in sensitive materials and therefore makes the analysis of organic materials even more challenging!

The aim of this review is to explore the possibilities and limitations of current analytical electron microscopy in the characterisation of organic interfaces, and to discuss the different methodological approaches that are necessary to overcome challenges such as poor materials contrast, or the significant damage to organic samples, which has to date severely limited the chemical information obtained. We consider two examples taken from the fields of biology and physics; the organic-mineral interface in bone, and the interface between organic donor and acceptor molecules in OPV devices. Both systems consist of domains with hierarchical structures, which require structural and chemical characterisation on a range of length-scales in order to gain an understanding of the

material architecture, function and properties. We begin by providing an overview of the variety of analytical techniques available in the TEM. The following two sections deal with each system separately, and consist of a brief background to the characterisation question and a discussion of recent analytical TEM studies. For more comprehensive material-oriented reviews, the reader is referred elsewhere [6, 7]. Finally, we summarise the commonalities and differences between characterisation approaches in these two systems, and discuss the challenges and directions for future organic interface studies.

2. Analytical TEM

Inelastic scattering of incident fast electrons occurs as a result of interactions with atomic electrons in the sample. These interactions include the excitation of collective oscillations such as plasmons or phonons, as well as the promotion of an atomic electron from an occupied to an unoccupied electronic state. The energy lost by the fast electron (corresponding to the energy gained by the sample) can be measured directly using a post-specimen spectrometer in a process known as electron energy-loss spectroscopy (EELS). Energy-losses up to ~50 eV correspond to collective excitations and transitions from valence or semi-core levels, while higher energy-loss events arise from transitions from core electronic levels. The information available in these regions is detailed in Table 1. Meanwhile, secondary processes may also occur in which the excited state relaxes by emission of an X-ray photon. The photon energy, which is characteristic of the element probed, is measured using energy-dispersive X-ray (EDX) analysis. The intensity of both EELS and EDX signals are proportional to the number of atoms of a particular element that is present in the sample, and therefore both can provide *quantitative* elemental information. Additionally, the fine structure present in EEL edges can be used to identify different local bonding environments and chemical states of the atom. Structure within the first ~50 eV of the edge onset is known as energy-loss near-edge structure (ELNES). ELNES is analogous to X-ray absorption near-edge structure (XANES), also known as near-edge X-ray absorption fine structure (NEXAFS), which is measured using X-ray absorption rather than fast electron scattering [8]. Currently the highest spatial resolution offered by soft X-ray microscopy is 10 nm[9], limited by the ability to fabricate the zone plates which focus the probe. While electron microscopes are capable of forming sub-angstrom probes, the spatial resolution of EELS measurements in organic samples is reduced by a) the delocalisation of inelastic scattering (which can be ~5 nm for low energy-loss transitions[10]) and b) electron-beam damage which varies with parameters such as beam current, accelerating voltage, specimen temperature and the ratio of the collected signal versus the number of electrons incident on the sample[11]. Compared to the electron microscope, XANES provides a combination of high energy resolution and low sample damage which has been shown to be extremely powerful for the study of functional groups in organic systems e.g. proteins and polymers [12, 13].

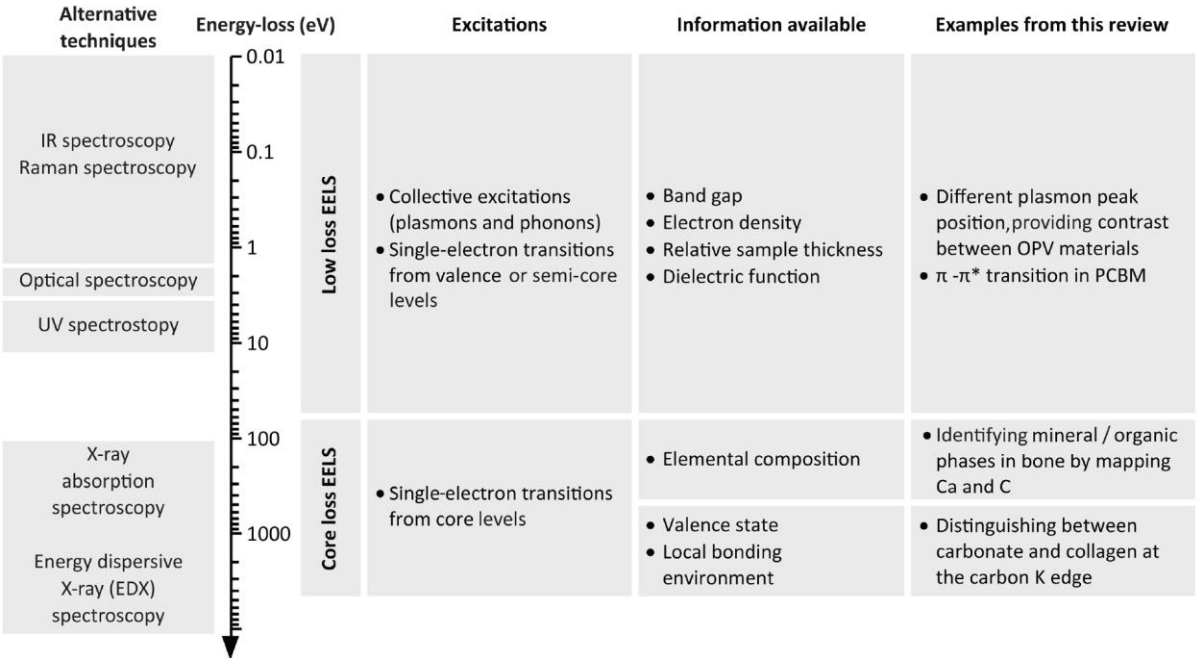

Table 1. Detailing the range of information which may be obtained using low loss and core loss EELS, as well as corresponding photon spectroscopy techniques.

An electron energy-loss spectrum (EELS) displays the intensity of scattered electrons as a function of energy-loss (figure 1a). EEL spectra can be acquired at each position as a scanning transmission electron microscopy (STEM) probe is rastered over the specimen. In this way a three-dimensional data-cube (two spatial dimensions and one spectral dimension) is built up, which is known as an EELS spectrum image (EELS SI, figure 1b). Alternatively, energy-filtered TEM images can be formed using only electrons which have lost certain energies. These electrons are selected using an energy slit, often between 1 and 10 eV in width. For quantitative analysis at core-loss edges, a “three-window method” is used. Two “pre-edge” images are collected in order to fit the background signal, and one “post-edge” image measures the intensity above the ionization edge (figure 1c). A larger series of EFTEM images may also be acquired forming a similar 3D data-cube known as an EFTEM SI, or electron spectroscopic image (ESI) (figure 1d). EFTEM SI provides a convenient method to map large sample areas with high spatial resolution. However, the total dose received by the sample increases with the acquisition of each EFTEM image. Therefore, if high spectral resolution is required (for improved background modelling, peak fitting or resolution of spectral features), it is often more appropriate to use the alternative data acquisition sequence provided by STEM-EELS spectrum imaging.

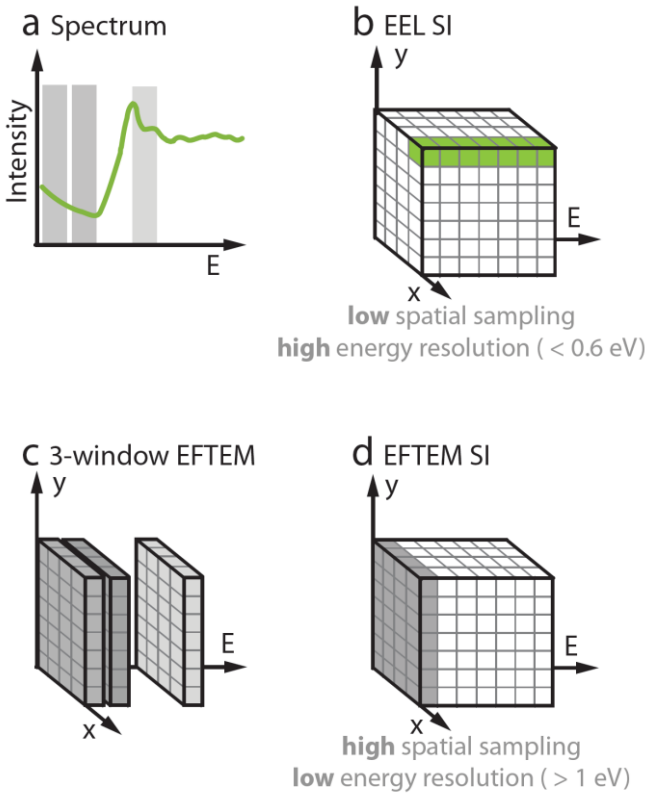

Figure 1. (a) EEL spectrum and (b) EEL spectrum image, in which a whole EEL spectrum is acquired at each pixel while the STEM probe is rastered over the specimen. (c) Two pre-edge EFTEM images are displayed as dark grey regions in (a) and (c), while the post-edge EFTEM image is light grey. (d) EFTEM SI in which a series of energy-filtered images are acquired sequentially. The two spectrum imaging techniques differ in spatial sampling and typical energy resolutions achievable (b and d).

3. Mineralised tissues

In the field of medicine, an increased understanding of the structure of mineralised tissues is hoped to facilitate the development of therapies to treat an increasing number of bone-related pathologies in our ageing society. Additionally, these tissues are of interest to the materials scientist as their sophisticated compositions and hierarchical architecture result in a highly improved material benefiting from the elasticity of collagen and the strength of mineral – the building blocks of these materials.

While the structure of mineralized biological tissues are well known at the macro- and micrometre scales, current studies have been aimed at increasing our understanding of the *nanoscale* structure and chemistry of these complex systems [14, 15]. Analytical TEM has already played a large role in the current understanding of bone at the nanometre scale and further TEM studies will play an important role in answering remaining questions about: a) the mechanisms of bone mineralisation (in particular the evolution of mineral and the role of the collagen template) b) the 3D arrangement and chemistry of mature collagen-mineral composite at the nanometre scale, c) nanostructure as a function of anatomical location and species and d) nanoscale modifications to structure and chemistry and their significance in common skeletal disorders such as osteoporosis.

3.1 Nanoscale structure of bone

Bone is composed primarily of two components: the mineral bioapatite, and type-I collagen fibrils. Bioapatite is a carbonated form of hydroxyapatite ($Ca_5(PO_4)_3OH$) with other possible chemical substitutions [16, 17]. Collagen displays a distinctive banding pattern due to the quarter staggered arrangement of collagen molecules within a fibril (figures 2,3). In this review, regions ~40 nm in length which appear dark in bright-field TEM (and bright by dark-field STEM) are referred to as 'gap regions' (figure 3) [18]. 'Overlap regions' are ~27 nm long and appear bright in bright-field TEM [14, 18]. The origin of this contrast is the presence of electron-dense bioapatite crystals in the gap regions (figure 2a) giving rise to greater scattering, and correspondingly a larger value of t/λ (thickness over mean-free-path of inelastic scattering). However, bioapatite may also be located between collagen molecules *within* a fibril (figure 2b) or completely outside of the fibril (extrafibrillar mineral) [14, 18]. The association of mineral and organic components is important in determining the properties of bone, and the detailed distribution of mineral within collagen has been revealed in a number of recent TEM studies [14, 15].

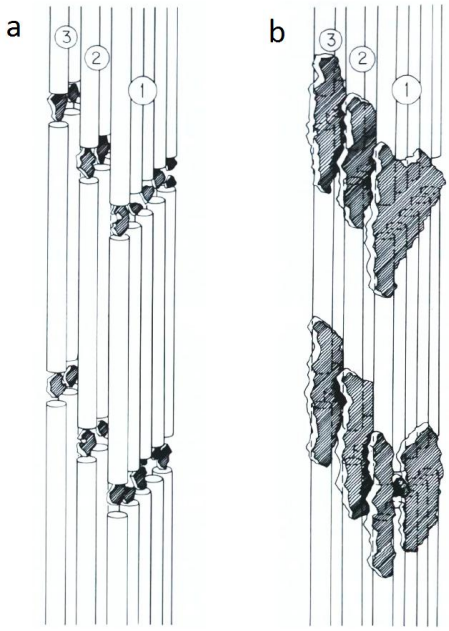

Figure 2. Simple model for packing collagen molecules in bone, as first presented by Hodge & Petruska [19]. (a) Collagen molecules are stacked end-to-end with a ~40 nm 'gap' between them (not drawn to scale). The stacking of adjacent molecules within a fibril is quarter-staggered. Three quarter-staggered arrangements are shown. Bioapatite crystals are postulated to nucleate and grow within the gap spaces. (b) Bioapatite is also postulated to grow into the intermolecular spaces within a fibril in the later stages of mineralisation [19]. From Landis *et al*. [18]

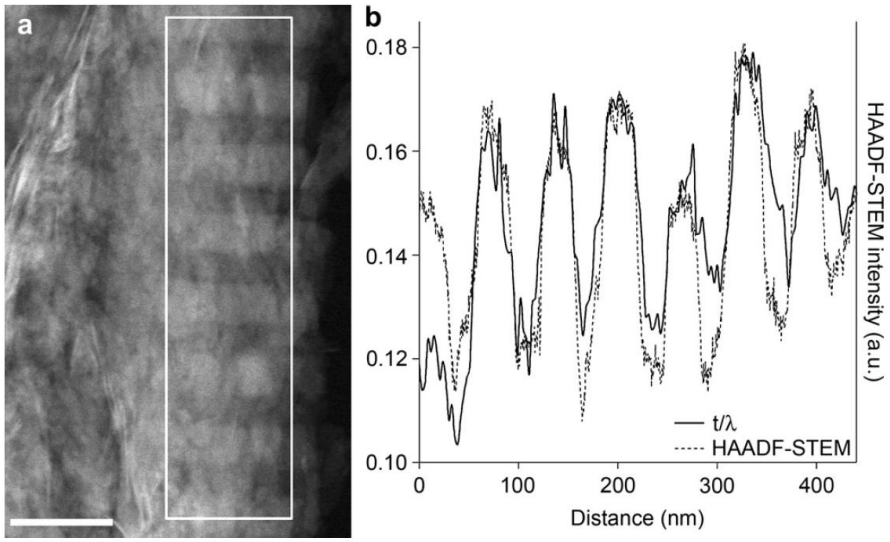

Figure 3. a) HAADF-STEM image of the collagen banding (scale bar = 100 nm) and b) corresponding t/λ profile (the HAADF-STEM intensity profile is shown as the dotted curve for reference). From [15]

Measuring bioapatite concentrations by TEM can be challenging due to difficulties with sample preparation [7, 14]. For example, mineralised samples prepared for TEM *via* aqueous processing and chemical fixation could suffer from structural changes to the collagen, and dissolution/re-precipitation of the bioapatite [14, 16]. The requirement for preservation of both organic and mineral components can lead to complex sample preparation techniques such as high pressure freezing and freeze substitution [7, 20]. Additionally, the creation of electron transparent samples *via* ultramicrotomy, focused ion beam (FIB) milling or polishing and ion milling each have limitations especially in the challenging case of a soft-hard biocomposite. A detailed review of current sample preparation protocols for mineralised tissues has been published by Klosowski *et al*. [7].

In the following section, we will consider the following aspects of bone characterisation in terms of insights that have been, or have the potential to be, obtained using analytical electron microscopy:

1. Nanoscale distribution of mineral with respect to the organic matrix,
2. Chemical composition of the mineral phase, and nature of substitutions,
3. Chemical composition of the organic phase.

3.2 Nanoscale structure by elemental mapping

Elemental profiles have been used to reveal the nanoscale structure of the mineral-organic arrangement. This has involved collecting STEM-EELS spectrum image datasets from longitudinal sections of collagen in a range of mineralised tissues [14, 15]. The distribution of elements is then calculated by integrating the signal from the relevant core-loss edges, and used to give both qualitative and quantitative information on the location of mineral with respect to collagen structure. In a STEM-EELS study of ivory dentine by Jantou-Morris *et al.* [15], P, Ca and O signals were found to be highest in the gap regions and lowest in the overlap regions, which is consistent with an increased content of bioapatite within gap regions (figure 4). Alexander *et al*. used STEM-EELS to quantify the distribution of mineral within mineralised tissue, in this case resin-embedded

mouse bone [14]. By integrating the Ca $L_{2,3}$ signal at different positions along a thin longitudinal section of collagen fibrils, they found that the ratio of Ca at overlap regions compared to gap regions was $R_{Ca\text{-}L}$ = 0.66 (*i.e*. approximately 50% more Ca was present in gap regions compared to overlap regions). However, as these STEM-EELS signals are 2D projections through a complex 3D structure, the absolute quantification of Ca within fibrils was not possible using STEM-EELS alone. If, for example, any *extrafibrillar* apatite was present at the point sampled by the STEM probe, it would contribute to the Ca signal and alter the gap:overlap ratio. To overcome this projection limitation, the 2D EELS data were combined with a steric model which estimated the packing density of bioapatite within gap channels. Using this combined EELS and modelling approach, Alexander *et al*. were able to refine the limits of bioapatite distribution within bone to ≤ 42% in gap channels, ≤ 28% in intermolecular overlap regions, and the remaining ≥ 30% of mineral in the extrafibrillar space [14].

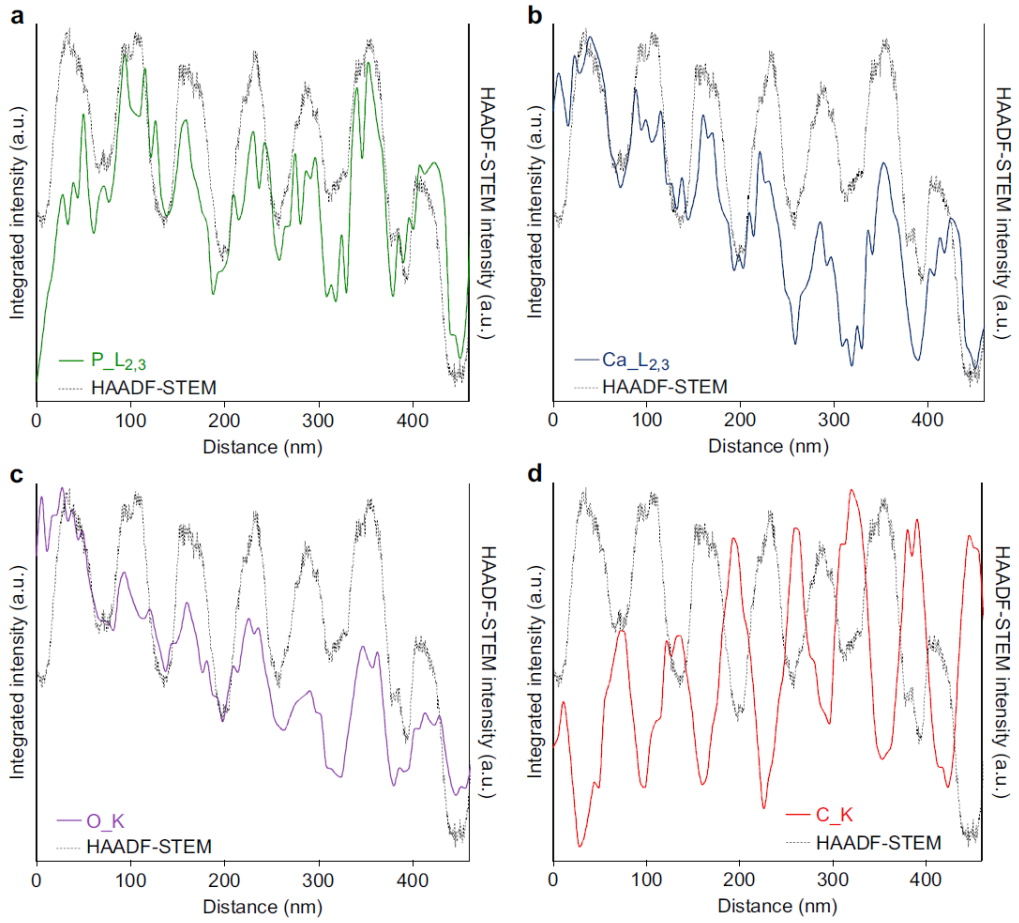

Figure 4. Signal intensity profiles across the banding of a) phosphorus $L_{2,3}$, b) calcium $L_{2,3}$, c) oxygen K and d) carbon K edges. The black dashed line is the corresponding HAADF-STEM image intensity [15].

3.3 Substitutions in the mineral phase

The stoichiometry of bioapatite is of interest as the presence of substitutions within apatites has an important influence on the physical properties of the mineralised tissue [21]. Elemental analysis has also been used in this case to evaluate the degree of substitution within bioapatite by quantifying the ratio between two elements using EELS, or often EDX [21-23]. For example, in an EDX study of

mineralised dental tissues by Srot *et al.*[21], peritubular dentine was found to contain a significantly lower Ca/P ratio (and higher and variable Mg/P) compared to intertubular dentine, which was taken as evidence that magnesium partially substitutes for calcium in the mineral. Care should be taken when quantifying Ca/P ratios in the TEM, as they are known to be altered by electron beam damage [21, 24]. Srot *et al.* report a larger loss in Ca compared to P in mineralised dental tissue [21]. In contrast to this, a comprehensive damage study on synthetic hydroxyapatite (HA) powder by Eddisford *et al*. observed an *increase* in the Ca/P ratio with electron fluence (and hence damage), corresponding to a larger loss of P that was also accompanied by a loss in O [24]. The damage in HA was found to be radiolysis-dominated *i.e.* greater damage was observed at lower accelerating voltages [24]. Eddisford *et al*. hypothesised that a mechanism exists to convert the radiolytic energy into kinetic energy and momentum of atomic nuclei, in order to explain the removal of P and O. Ultimately, melting and transformation to cubic calcium oxide was observed under intense electron irradiation n[24]. Cooling had only a small effect on damage, which was also unexpectedly found to be fluence-rate dependent [24]. The damage behaviour of synthetic HA reported by Eddisford *et al*. is complex and incompletely understood. Additionally, the damage behaviour of synthetic HA is inconsistent with the damage reported in dental tissues. Further work is clearly needed to understand the detailed damage properties of different mineralised tissues. This study also highlights the importance of carefully controlling and reporting the accelerating voltage, dose and fluence rates used to quantify Ca/P ratios. The recent introduction of high solid angle EDX detectors [25] for more efficient EDX signal acquisition will be beneficial for elemental quantification studies such as this, as they require approximately three times less electron dose to collect a given EDX signal [26].

As well as the substitution of metal cations, which have been studied using elemental ratios, carbonate ions are known to substitute into the bioapatite structure. Carbonate groups may be present at a range of sites: replacing a hydroxyl group (A-site) or a phosphate group (B-site) in the crystal, or they may be located on the crystal surface (unstable C-site) [27]. As the element carbon is present within mineralised tissue in both the organic and mineral phases, *elemental* mapping would not be sufficiently selective to distinguish between substitutional carbonates and organic carbons. Discrimination of different local bonding environments is required, which can be achieved using electron energy-loss near edge structure (ELNES).

Figure 5 shows carbon K edge ELNES from mineralised ivory dentine [15] and tooth enamel [21]. The most intense feature at ~290.2 eV [15, 21] is assigned to carbonate groups. This peak is present in the area-averaged measurements from enamel exposed to both low and (unquantified) high electron doses [21], as well as the point spectra recorded from ivory dentine. The similar appearance of the carbonate peak in each case suggests that this feature is relatively stable under electron beam irradiation, while other regions of the spectrum undergo significant changes with increased electron dose. Therefore it is conceivable that the carbonate peak at 290.2 eV will be valuable in future work to quantify the degree of carbonate substitution with high spatial resolutions.

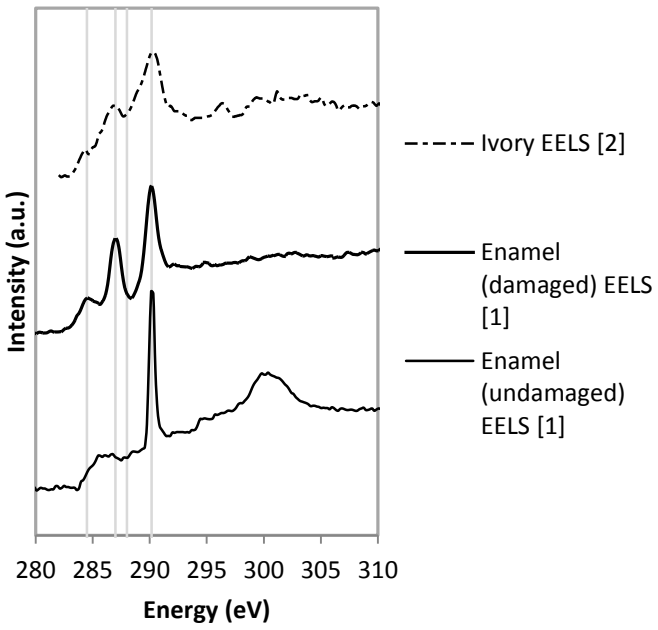

Figure 5. ELNES of carbon K edge from enamel samples [21] and ivory dentine [15]. Energy scales have been recalibrated to align the peak at 290.2 eV which is assigned to carbonate.

3.4 The organic phase

The organic phase in mineralised tissue is composed mainly of collagen [16] along with a few mass percent of non-collagenous proteins (NCPs). Although NCPs are known to play important roles in bone mineralisation and structure [28], their low concentrations make them more challenging to study, and we will limit the scope of this section to the majority component, collagen. Modifications in collagen molecules, and the associated changes in molecular cross-linking and collagen-mineral binding, are known to give rise to abnormal and dysfunctional tissues, as is the case in the *osteogenesis imperfecta* pathology (brittle bone disease) [29]. To gain a better understanding of how these modifications result in fragility at the whole-bone level, it would be advantageous to be able to characterise the chemical structure of collagen at the molecular level, particularly to establish which functional groups play an important role in the collagen-mineral binding. Such studies would also be useful in uncovering the mechanisms that control the process of tissue mineralisation.

Collagen molecules are composed of amino acids such as glycine ($C_2H_5NO_2$), proline ($C_6H_9NO_2$), and hydroxyproline ($C_5H_9O_3N$) [14]. To the best of our knowledge, high spectral resolution ELNES from collagen alone have not been reported in the literature. However XANES measurements, which probe analogous transitions using soft X-rays rather than fast electrons, are available for both collagen alone [30], as well as collagen within bone samples [31] (figure 6b,d). In the X-ray microscope, collagen exhibits a major peak at ~288 eV assigned to a 1s $\rightarrow \pi^*_{C=O}$ transition in carbonyl groups, along with a minor peak at 285 eV and the broad resonance at ~300 eV from the 1s $\rightarrow\sigma^*$ transition in C-C bonds [30].

In order to estimate the relative number of carbon atoms in collagen molecules compared to carbonate groups in the mineral phase, we consider a typical bone structure composed of 30 wt% collagen and 60 wt% bioapatite. Furthermore, if the bioapatite is substituted with 6 wt% carbonate

[32], we calculate that approximately 95% of the carbon atoms in mineralised bone will be present in collagen. This conclusion is supported by the observed opposite periodic trend of elemental C compared to Ca, P and O along mineralised collagen, in both ivory dentine (see figure 3) [15] and mouse bone [14], which is consistent with the majority of carbon being located outside of the mineral component. Although the majority of carbon within mineralised bone is contained in collagen, the predominant feature in the carbon K edge ELNES from ivory dentine is the *carbonate* peak at 290.2 eV, and no obvious peak at 288 eV from collagen can be observed (figure 6e). In contrast, Srot *et al.* observe features at 288 eV in area-averaged spectra from dental pulp, but not in enamel (figure 6f,g) which has a high mineral content of ~96% [32]. Apart from variations in the collagen content of different tissue types, the differences between reported results could also be due to a combination of different sample preparation protocols or effects of electron beam damage from the different operating conditions used. Despite this, the presence of features at 288 eV in the dental pulp sample is encouraging, and opens up the exciting possibility of detailed chemical analysis of collagen by EELS. However, the area over which spectra were acquired from this dental pulp sample is large, on the order of ~100 nm × 100 nm. Currently the same level of chemical information is readily available using XANES. In fact, the current spatial resolution limit of scanning transmission X-ray microscopy (STXM) is ~15 nm, which is however still too poor to resolve much (if any) sub-molecular information. Further work is necessary to establish the ultimate damage-limited spatial resolution for the analysis of collagen by EELS.

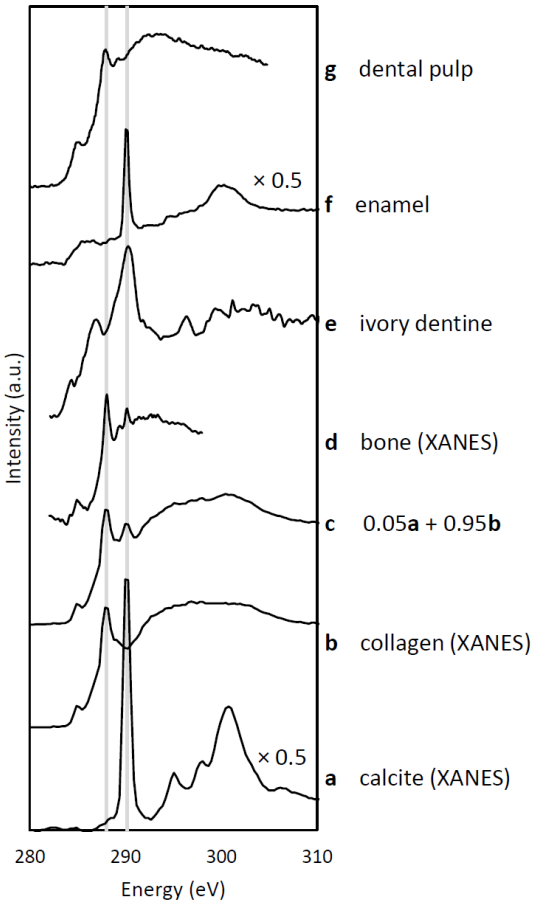

Figure 6. XANES of (a) calcite[33] reference material containing carbonate groups, (b) collagen[30], and (c) a linear combination of the two corresponding to a typical bone composition, which contains

similar features compared to (d) XANES spectrum from bone. ELNES from (e) ivory dentine[15], (f) enamel and (g) dental pulp[21] display variable carbonate and collagen-related peaks at 290eV and 299 eV respectively. All spectra have been realigned using the carbonate peak at 290.2 eV, and intensities have been normalised between 282 and 310 eV.

One possible damage reduction strategy is the use of low-loss EELS, which has the potential to provide chemical information with much less electron dose due to the larger interaction cross-section of these low energy transitions. Low-loss EELS spectra from mineralised tissue have been reported [15, 21], however the interpretation of the various features observed presents a significant challenge due to the difficulty of simulating low-loss transitions, and the complex nature of the biological systems. Nevertheless, Jantou-Morris *et al*. [15] have performed preliminary analyses to determine both thickness/density variations, and the calcium content by extracting the single electron-like features, including the Ca $M_{2,3}$ edge, using Kramers-Kronig analysis.

4. Organic Photovoltaics

Organic molecules and polymers hold great promise for next generation electronic and optoelectronic devices, owing to their advantages of low-energy and low-cost production, versatile synthesis processes and the ability to tailor their properties [34]. However, organic solar cells currently operate with efficiencies of ~5-10% [35], and must be developed further in order to compete with commercial inorganic power generation, such as silicon solar cells with >25% efficiencies [36]. The operation of an organic solar cell involves multiple processes which occur in the active layer in order to generate current. These include: (i) the absorption of a photon and creation of a strongly-bound exciton, (ii) exciton migration to the donor-acceptor interface, (iii) exciton dissociation into an electron and hole at the donor-acceptor interface, (iv) transport of the electrons and holes and (v) charge collection at the electrodes.

4.1 Structure of the bulk heterojunction

Due to the limited diffusion length of an exciton within the active layer (~10 nm) [37], and the desire to maximise the donor-acceptor interface for maximum exciton dissociation, a common architecture of the OPV active layer involves an interpenetrating 3D network of donor and acceptor phases with small domain sizes. This structure is known as the bulk heterojunction (BHJ) [38]. The 3D morphology of the BHJ, the molecular order within each domain, as well as the nature of the interfaces between donor and acceptor domains are all important parameters which control device efficiency [38]. For example, it is important that an electron or hole created at an interface is able to travel through a continuous percolating pathway to the corresponding electrode in order to generate current. Similarly, increased order and crystallinity within a domain can enhance the transport of charge carriers through it [39]. Investigation of such parameters requires analytical techniques with high spatial resolution. Many of the studies discussed below investigate BHJ thin films in an orientation whereby the electron beam travels perpendicularly through the film, providing information on the top-view domain structure integrated through the thickness of the film. However, as any photogenerated charge carriers must also move across the film thickness to reach the electrodes, the *vertical* domain structure is also key to device efficiency. Full characterisation therefore requires three-dimensional tomographic information and/or the fabrication of cross-sections to provide more detailed structural information of the interfaces, and which is also more appropriate for related multi-layered devices. The challenges of fabricating cross-

sectional samples is discussed in more detail by Gilchrist *et al.* [ref this issue]. Another key requirement of the characterisation technique is the ability to distinguish between the different components in an all-organic photovoltaic layer. However, as many of the components that make up OPV systems have similar elemental compositions, these samples suffer from inherently low contrast in the TEM. Strategies which have been employed to overcome these characterisation challenges will be discussed in the following sections.

4.2 Bright field TEM imaging

Early TEM studies of OPV active layers were performed by van Bavel *et al*. [40, 41] on BHJ structures composed of two commonly used OPV materials, the electron donor poly(3-hexylthiophene) (P3HT) and the fullerene derivative [6,6]-phenyl-C61-butyric acid methyl ester (PCBM) as the electron acceptor. Higher intensity fibrillar structures were observed in conventional bright field TEM images, which were identified as P3HT nanorods due to the lower density of crystalline P3HT at 1.1 g/cm^3 compared to PCBM at 1.5 g/cm^3 [40]. By acquiring TEM images at various film tilt angles, 3D reconstructions were created from which the authors also calculated that ~60% of the P3HT was present as crystalline nanorods. However, the quantitative interpretation of these BFTEM images is limited by a number of challenges, including the possibility of local density changes within domains [42] and, more importantly, the dominant contribution of phase contrast in these images. In order to image domains of ~10 nm in size, BFTEM images are often acquired under highly defocussed conditions. This results in selective enhancement and suppression of different frequency ranges, as well as contrast inversions, due to the oscillating nature of the contrast transfer function [43]. As well as the possibility of misinterpreting the true domain morphology [43], this contrast mechanism often does not satisfy the tomographic contrast requirement of a signal which varies monotonically with thickness [44]. The ambiguities in using BFTEM contrast to assign domains have been discussed in detail in a number of studies [43-46]. To overcome the limitations of BFTEM imaging, different contrast enhancement strategies have been employed, which all rely on *inelastic* scattering of the electron beam *i.e.* chemical contrast. A comparison between (zero-loss) TEM imaging and inelastic imaging is displayed in Figure 7, which also illustrates the effect of varying the energy-selecting slit position and the objective lens defocus on images acquired from the same region of a P3HT/PCBM BHJ sample. It is evident that these imaging conditions produce completely dissimilar contrast. The analytical TEM techniques which have been employed to enhance contrast in OPV systems include elemental mapping by EDX [47, 48] or core-loss EELS [48, 49], mapping variations in the plasmon peak position [42, 44, 45, 50-54] as well as single electron excitations in the low-loss region of the EEL spectrum [45].

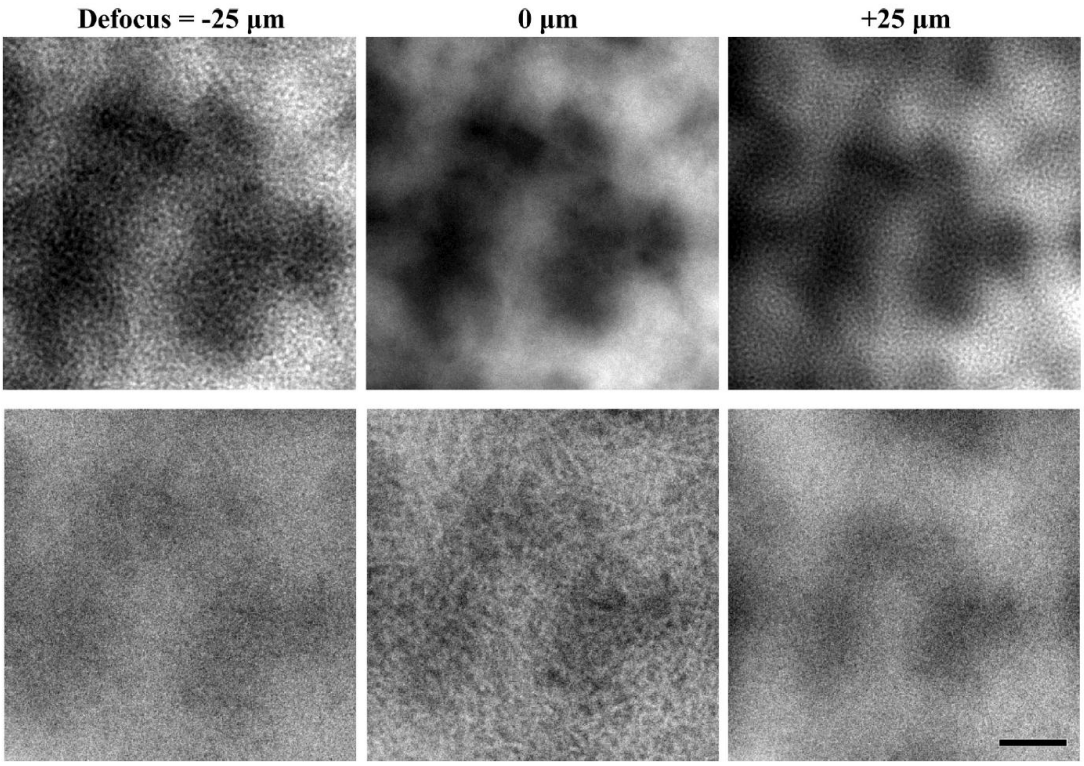

Figure 7. EFTEM images collected from the same area of a P3HT/PCBM film, using an energy selecting slit centred at 0 eV (top row) or 19 eV (bottom row). The columns (left to right) show images acquired with an objective lens focus of -25, 0, and +25 µm. The scale bar is 200 nm. Low-frequency thickness-related intensity variations can be observed in every image. Compositional contrast is more clearly revealed in the low-loss EFTEM image acquired at Gaussian focus. The features in this image are dissimilar to the high frequency features observed in zero-loss defocussed images. From [44].

4.3 Core-loss transitions and elemental maps

Elemental mapping has been applied to the P3HT/PCBM system [49], in which P3HT contains sulfur while PCBM does not. Core-loss EFTEM was used to distinguish between P3HT- and PCBM-rich phases through elemental mapping of carbon and sulfur [48, 49]. Using the three window EFTEM method at the sulfur $L_{2,3}$- and carbon K-edges (at 165 and 284 eV respectively), Kozub *et al*. [49] were able to image pure P3HT crystals (figure 8) as a function of annealing temperature, and to quantify the composition of the surrounding amorphous P3HT-PCBM matrix. Mapping of different domains by core-loss EELS or EDX does not necessarily require the presence of an element in one phase but not the other. This was demonstrated in a study of copper phthalocyanine (CuPc)/C_{60} bilayers by Gilchrist *et al*. [47]. As C_{60} contains a greater concentration of carbon compared to CuPc, differing carbon mass percentages were successfully used to distinguish phases through STEM-EDX spectrum imaging, and also to determine the location and roughness of the interface [47].

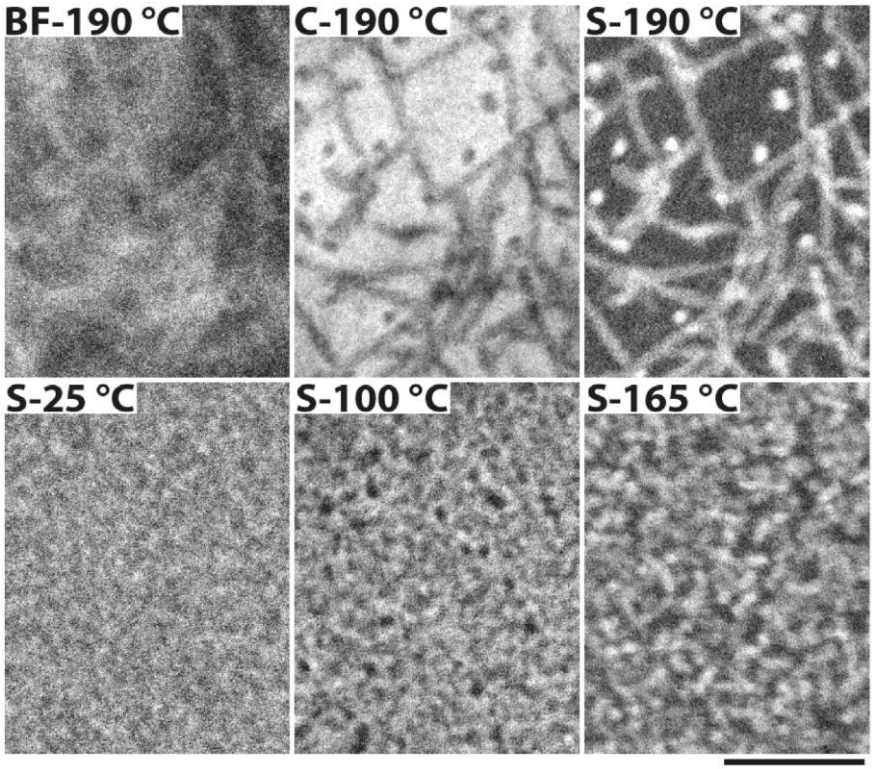

Fig. 8 Core-loss EFTEM analysis of annealed P3HT/PCBM films. Top row, left to right: Bright field TEM image (BF) and elemental maps of carbon (C) and sulfur (S) for a film annealed at 190 °C. Bright regions in the sulfur map correspond to P3HT-rich domains. Bottom: Sulfur maps showing different domain structures for films annealed at 25 °C, 100 °C, and 165 °C. Scale bar is 200 nm. From [49].

4.4 Low-loss transitions: bulk plasmons

The use of inner-shell transitions for elemental mapping has proved successful in enhancing contrast in a range of OPV samples. However, possibly due to the low cross-sections of inner-shell excitations, which require high electron doses for good signal to noise [43], it is the *low-loss* transitions that have been far more extensively employed for OPV characterisation. The majority of low-loss studies rely on variations in the energy of the bulk plasmon between different phases to provide contrast [42, 44, 45, 50]. Other features such as single-electron transitions which also occur in the low-loss region (such as the π to π^* transition at ~ 6 eV in PCBM) have also been studied, but to a lesser extent [50].

A number of approaches have been used to sample the variations in the bulk plasmon across a sample. The simplest approach records a single EFTEM image, which has been shown to provide material contrast. Drummy *et al*. used a 19 ± 4 eV energy window to identify P3HT (bright) and PCBM (dark) domains [42] (figure 9). The single energy-loss image was used to separate the two phases by thresholding (figure 9e), and the segmented image was used to quantify fibril diameters and the sizes of PCBM-rich regions. They found that a second image at 30 ± 4 eV gave inverted contrast which was used to unambiguously assign the two phases. In order to emphasise the P3HT domains within P3HT/PCBM layers, ratios between two EFTEM images collected at 19 and 29 eV have also been calculated by Herzing *et al*. [51] EFTEM imaging at 19 eV has also been used to collect tomography series, and to reconstruct the 3D morphology of domains within P3HT/PCBM films [44]. Due to the non-linear dependence of both the single and multiple plasmon scattering probabilities

with sample thickness, especially problematic at high tilt angles or where t/λ > 0.5 [55], a refined methodology for tomography using plasmon EFTEM imaging has been presented by Mendis *et al*. [55] This method acquires two additional EFTEM images at each tilt angle: an unfiltered image I_t and an "elastic" image I_0 which is acquired with a 10 eV slit at the zero loss peak. These images are used to calculate local sample thickness (t/λ), enabling the plasmon-loss images to be corrected for thickness effects. In a related effort, Pfannmöller *et al*. [46] have also applied a normalisation procedure, which involves dividing all spectra by the integrated intensity under the low loss region, (in this case 2-30 eV) to remove the effects of thickness on individual EFTEM images extracted from an EFTEM SI (see figure 1).

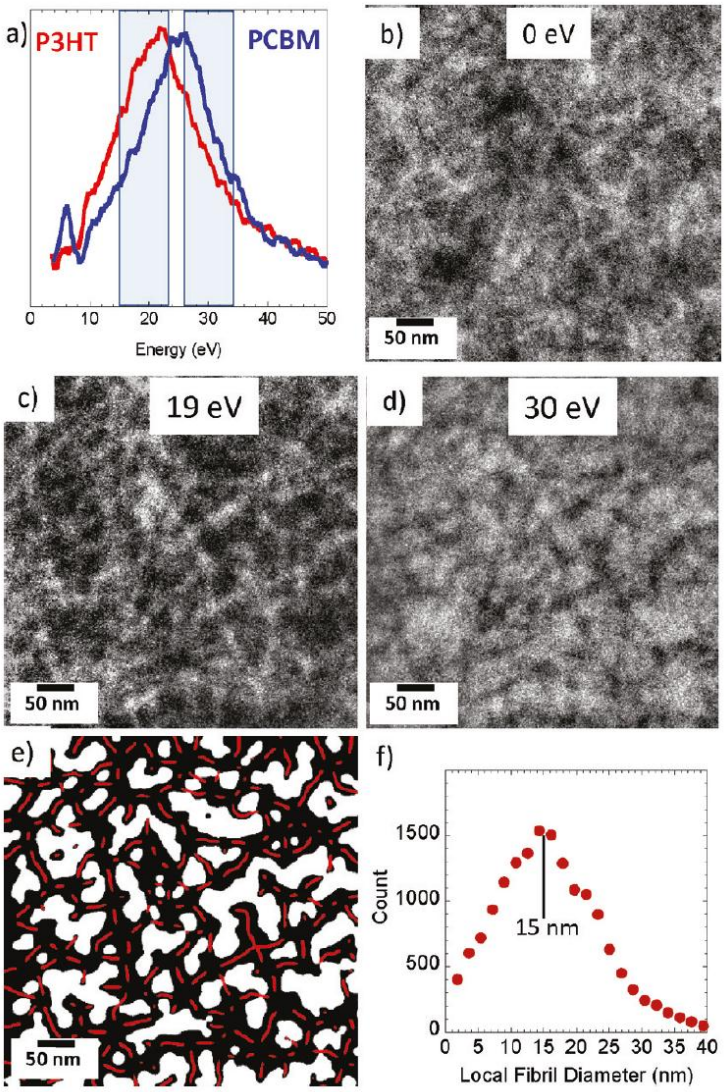

Figure 9. EFTEM analysis of a 100 nm thick of P3HT/PCBM blend. (a) EELS spectra from pure P3HT and pure PCBM films, with energy windows at 19 ± 4 eV and 30 ± 4 eV, where spectral differences between materials are most apparent. (b) Zero-loss image, (c) 19 eV image (P3HT rich domains are bright) and (d) 30 eV image (PCBM domains are bright). (e) Segmented image created using a threshold method on image (c), with skeleton of fibrils overlaid in red. (f) Distribution of fibril diameters (15 ± 8 nm) calculated from (e). From [42].

The same two-window technique applied by Herzing *et al*. has also been used recently by Gu *et al*. [53] to characterise a ternary blend consisting of two polymers (P3HT and poly[2,6-(4,4-bis-(2-ethylhexyl)-4H-cyclopenta[2,1-b;3,4-b']dithiophene)-alt-4,7-(2,1,3-benzothiadiazole)] (PCPDTBT)) as well as PCBM. While PCBM was successfully distinguished from the donor polymers, the two-window method was unable to distinguish *between* the polymers P3HT and PCPDTBT due to their similar plasmon peak positions. In this study it is unclear whether the limiting factor was materials-based, *i.e*. due to the inherent similarity in bulk plasmon energy of the two materials, or whether the low spectral sampling of the EFTEM SI limited the characterisation.

4.5 Towards improved spatial resolution and quantification

The studies discussed above demonstrate the ability of spectroscopic imaging in characterising the morphology of BHJ domains, on length scales of ~10 nm. Domain structure at this length scale is important, for example, in charge carrier transport and collection at electrodes. At finer length scales, BHJ structure *at the molecular level* is critical for processes such as exciton dissociation. The assignment of domains using one and two-window EFTEM methods involves an implicit assumption that the BHJ may be modelled as a simple binary system consisting of two homogeneous phases separated by abrupt boundaries. However more complexity may exist, for example if a mixed phase forms a third domain alongside homogeneous phases [45]. In order to be sensitive to more complex interfaces, a fuller range of spectral information must be sampled to offer more discriminative power. A number of recent studies have employed EFTEM SI, from which parameters such as plasmon peak positions have been extracted [50]. Alternatively, datasets may be considered as a whole using multivariate statistical analysis. These techniques are used to find distinct spectral motifs within the dataset, in an automatic or semi-automatic fashion, and can classify regions in the sample containing similar spectral features without prior knowledge of reference compounds, and with reduced experimenter bias. Additional information on multivariate statistical techniques may be found in dedicated papers [56, 57].

The evidence of mixed phases by imaging and spectroscopy in the TEM is sparse and somewhat conflicting [44, 45, 50]. For example, both Herzing *et al*. [44] and Pfannmöller *et al*. [45] have studied interfaces in P3HT/PCBM films *via* EFTEM SI. Using principal component analysis (PCA) of low-loss datasets, Herzing *et al.* [44] found no evidence of intermixing (from analysis of the limited number of principal components which were required to reproduce the spectral features). However a different *non-linear* multivariate statistical analysis approach used by Pfannmöller *et al*. [45] identified three distinct classes of spectra (figure 10a,d). The third class of material was interpreted as evidence of a "blend" phase which formed a boundary between the P3HT and PCBM-rich domains, and which decreased in size upon annealing at 120 °C. The conflicting findings of these two studies were attributed to the choice of different data analysis routines. However, differences may also arise from variations between sample preparation routes, EFTEM imaging parameters, or operating voltage (80 kV and 200 kV for Herzing *et al.* and Pfannmöller *et al.* respectively) imparting different amounts of beam damage to the sample. As the total dose was not stated, it is difficult to draw definitive conclusions on the validity of each result.

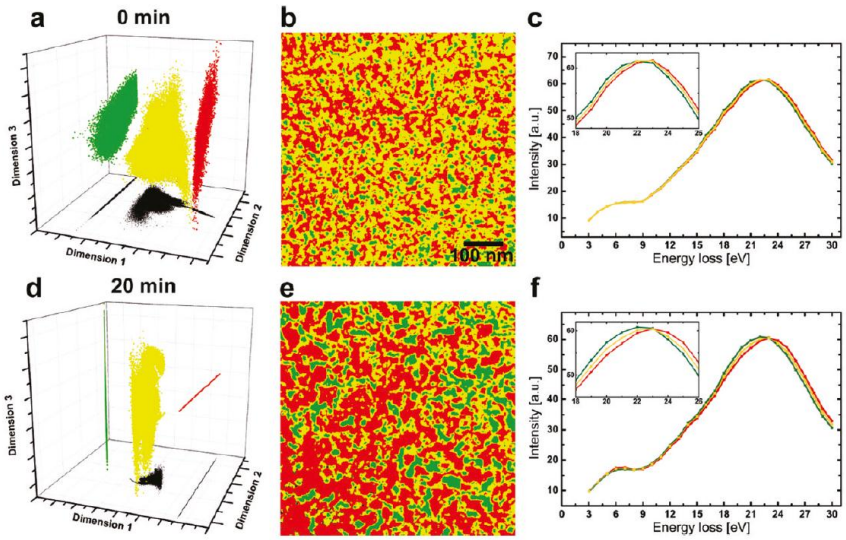

Figure 10. Non-linear multivariate statistical analysis of EFTEM SI collected from P3HT/PCBM films before (top row) and after (bottom row) annealing. Three separated clusters are identified in scatterplots (a, d). The spatial distribution of each cluster is displayed in (b and e), and members of the yellow cluster are consistently found to create an envelope around other class areas. Therefore regions marked in yellow are assumed to be intermixed regions. This phase is larger in the pristine layer. ESI spectra of the three classes averaged over all assigned pixels (c, f) show that the three clusters exhibit different plasmon energies. From [45].

A detailed study on effect of intermixing on the low-loss spectrum has been carried out by Schindler *et al*. [50] using C_{60}/zinc phthalocyanine (ZnPc) systems (figure 11). The plasmon peak position was recorded as a function of film composition. For each composition, two samples were fabricated: a bilayer sample with differing thicknesses of C_{60} and ZnPc, as well as blend structure. They found that plasmon peak positions in the bilayer samples were in good agreement with peak positions calculated from superpositions of the individual component spectra (figure 11b). It is worth noting that the graph of plasmon peak centre versus bilayer composition is non-linear due to the different shapes of the plasmon peaks of C_{60} and ZnPc (*i.e.* the narrower C_{60} plasmon). More importantly, however, plasmon peak positions were found to be consistently lower in the blend structures compared to bilayers. This result demonstrates the difficulty in assigning a definitive material composition at the interface, due to the non-negligible effect of mixing on plasmon spectra.

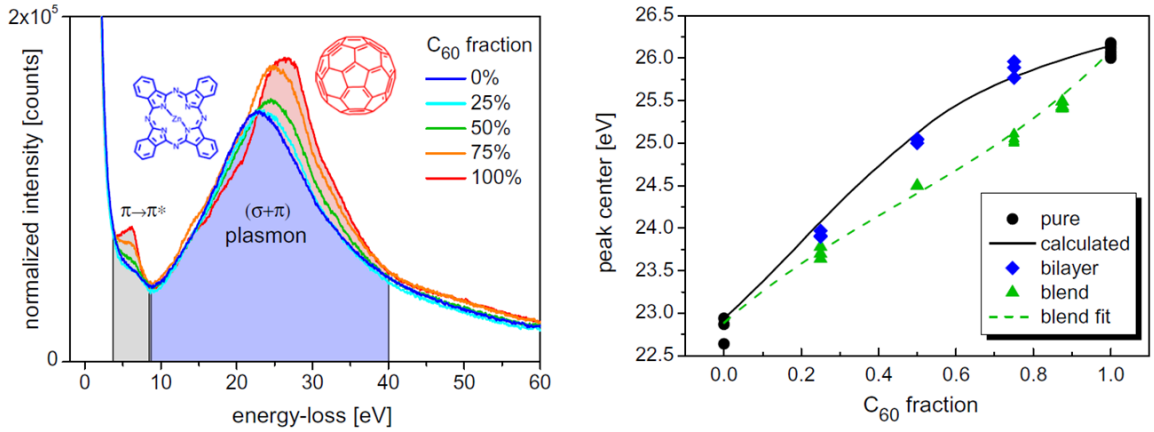

Figure 11. Analysis of the plasmon peak position as a function of composition and intermixing. (a) EELS of 40 nm thick layers of pure ZnPc (blue), pure C_{60} (red) and their blends. The position of the (σ + π) plasmon shifts with increasing C_{60} fraction. (b) Plasmon peak positions as function of C_{60} fraction. Pure ZnPc and C_{60} layers are plotted as black circles, and superpositions of the pure spectra are plotted as the solid curve. Experimental bilayer values are plotted as blue diamonds, while the plasmon blends (triangles) exhibit lower energy bulk plasmons. From [50].

Most recently, rather than using EFTEM SI, Guerrero *et al*. [54] have used the alternative data acquisition sequence of STEM-EELS SI to analyse aged cross-sections of P3HT/PCBM layers within whole devices. They were able to acquire a 3D EELS dataset using just 3×10^4 electrons/nm^2, which is two orders of magnitude lower than typical doses which have previously been used to acquire EFTEM SI of OPV samples [45, 50]. As well as the advantage of lower electron doses, and hence less beam damage, using EELS SIs makes full use of the energy resolution of the instrument (spectral energy resolution in an EFTEM SI is degraded by the convolution with a comparatively large energy selecting slit). Larger energy ranges can also be studied more easily without requiring additional electron dose, simply by adjusting the dispersion of the spectrometer. In this way the energy range studied by Guerrero *et al*. was 0-90 eV (compared to typical ranges of 0-30 eV by EFTEM SI).

4.6 Limitations of plasmon imaging, and the rest of the low loss spectrum

A number of studies observe that the plasmon peak remains fairly constant over prolonged periods of electron beam exposure [44, 46], making it suitable for reliable identification of phases. However, electron beam irradiation can change the population of valence electrons which in turn would shift the plasmon peak energy [58]. Therefore care is required if high doses are applied to the sample, as would be the case in 3D tomography.

As observed earlier in the ternary blend study by Gu *et al.* [53], plasmon peak positions do not always differ by large enough amounts to allow different components (*e.g.* P3HT and PCPDTBT) to be distinguished. In this situation, additional features corresponding to optical and UV transitions (in the energy region ~1-8 eV) may be useful for identifying different species, especially as donor and acceptor materials are often selected for their differing optical characteristics, in an attempt to cover the full UV-vis range. Pfannmöller *et al*. [45] have already demonstrated the ability to recreate maps of P3HT/PCBM using a reduced set of EFTEM images, between 3 and 10 eV. While they found

remarkable agreement with plasmon-based mapping from the full EFTEM SI (3-30 eV), the reduced dataset did result in noisier maps. This strategy may be improved by utilising STEM-EELS acquisition rather than EFTEM SI, which provides more spectral information per unit electron dose due to the higher efficiency of the acquisition sequence. Additionally, the use of *monochromated* EELS would further increase the spectral resolution and reduce the background arising from zero loss peak tails, making new features in this energy range visible.

A study of P3HT/PCBM by Pfannmöller *et al*. [46] reported a peak at 2.65 eV corresponding to a P3HT optical absorption. This peak was found to disappear after a dose of 10^5 electrons/nm^2 (using 60 kV electrons). Other peaks at 3.63 eV and 6.52 eV from PCBM seemed to remain stable throughout the exposure. In a different study, Herzing *et al*. found the 6.6 eV peak to decrease in intensity and shift to a slightly lower energy-loss value with increasing (but unquantified) dose of 80 kV electrons. Therefore the success of this approach will depend upon the resistance to beam damage of the specific material, and finding optimal operating conditions to minimise the effects of this damage.

5. Discussion and conclusions

The analytical TEM studies undertaken to date have provided successful characterisation of organic domains on length scales of ~ 10 nm. In mineralised tissues, these techniques have provided insights into the structure of the mineral-organic arrangement at the fibrillar level, such as the increased amount of Ca and P within gap regions [15], and the gap:overlap:extrafibrillar distribution of bioapatite [14]. Analytical TEM has also provided proof-of-principal mapping of the chemical composition of the mineral phase, through both elemental analysis as well as ELNES of carbonate groups (at high spatial resolution).

In the organic phase, detailed chemical information (*via* ELNES) has been achieved, but only by compromising spatial resolution. In further work, there is still a need to improve upon the spatial resolution of collagen mapping, for example to realise molecular scale mapping of functional groups within collagen molecules or bone nucleating proteins such as osteonectin. While improvements in detector efficiencies can be expected to contribute to improved damage-limited spatial resolutions, we also require a better understanding of the damage behaviour in these complex systems. For example, the optimum acquisition conditions will vary greatly for a material which displays a damage recovery process compared to one that does not, as fluence *rate* will become an important parameter as was reported in hydroxyapatite [24].

Another future challenge is to apply these techniques to clinically relevant questions, such as the effect of age or disease on the structure of mineralised tissue. Such studies will require large sample sizes (often n>10) to ensure a statistically relevant analysis of variable biological specimens. Therefore, it is likely that some degree of correlation between high-resolution analytical techniques and high-throughput techniques such as Raman spectroscopy or Fourier transform infrared spectroscopy (FTIR) will be useful.

In the case of OPV, analytical TEM has revealed the larger-scale morphology of domain structures within an OPV active layer. Characterisation has mainly been carried out using the low-loss transitions, which provide the highest cross-sections and therefore better signal for a given electron dose. Plasmon mapping has been used to great effect to enhance contrast from domain

morphologies, and studies are moving towards greater spectral information in the form of EFTEM SI and EELS SI. However, quantitative characterisation of the interface between donor and acceptor domains, at the molecular level, remains elusive. Interpreting plasmon peak positions can be difficult at domain boundaries where intermixing affects the spectra. Additionally, the spatial resolution of plasmon mapping is limited by the localisation of these collective oscillations, which is on the order of ~2 nm [55]. This also illustrates the difficulty of applying low-loss spectroscopy to complex systems. Overall, analytical TEM has provided a wealth of structural and chemical information on these various organic systems. A greater understanding of damage effects, improvements in detector efficiencies, and increased use of efficient, high spectral resolution analysis modes will be important in future discoveries in these materials.

The authors gratefully acknowledge funding from ERC starting investigator grant #257182.

References

[1] Terauchi M, Tanaka M, Tsuno K, Ishida M. Development of a high energy resolution electron energy-loss spectroscopy microscope. Journal of Microscopy-Oxford. 1999;194:203-9.
[2] Muller DA, Kourkoutis LF, Murfitt M, Song JH, Hwang HY, Silcox J, et al. Atomic-scale chemical imaging of composition and bonding by aberration-corrected microscopy. Science. 2008;319:1073-6.
[3] Kimoto K, Asaka T, Nagai T, Saito M, Matsui Y, Ishizuka K. Element-selective imaging of atomic columns in a crystal using STEM and EELS. Nature. 2007;450:702-4.
[4] Suenaga K, Tence T, Mory C, Colliex C, Kato H, Okazaki T, et al. Element-selective single atom imaging. Science. 2000;290:2280-+.
[5] Ramasse QM, Seabourne CR, Kepaptsoglou DM, Zan R, Bangert U, Scott AJ. Probing the Bonding and Electronic Structure of Single Atom Dopants in Graphene with Electron Energy Loss Spectroscopy. Nano Lett. 2013;13:4989-95.
[6] Chen LM, Xu Z, Hong ZR, Yang Y. Interface investigation and engineering - achieving high performance polymer photovoltaic devices. J Mater Chem. 2010;20:2575-98.
[7] Klosowski M, Porter AE, Shefelbine S, McComb DW. Analytical Electron Microscopy of Bone and Mineralized Tissue. In: Neu CP, Genin GM, editors. Handbook of Imaging in Biological Mechanics: CRC Press; 2015. p. 579.
[8] Goode AE, Porter AE, Ryan MP, Wirick S, McComb DW. Correlating EELS spectrum imaging with x-ray microscopy. EDGE 2009 Poster2009.
[9] Chao W, Fischer P, Tyliszczak T, Rekawa S, Anderson E, Naulleau P. Real space soft x-ray imaging at 10 nm spatial resolution. Opt Express. 2012;20.
[10] Egerton RF. Limits to the spatial, energy and momentum resolution of electron energy-loss spectroscopy. Ultramicroscopy. 2007;107:575-86.
[11] Egerton RF. Control of radiation damage in the TEM. Ultramicroscopy. 2013;127:100-8.
[12] Hitchcock AP, Dynes JJ, Johansson G, Wang J, Botton G. Comparison of NEXAFS microscopy and TEM-EELS for studies of soft matter (vol 39, pg 311, 2008). Micron. 2008;39:741-8.
[13] Ade H, Hitchcock AP. NEXAFS microscopy and resonant scattering: Composition and orientation probed in real and reciprocal space. Polymer. 2008;49:643-75.
[14] Alexander B, Daulton TL, Genin GM, Lipner J, Pasteris JD, Wopenka B, et al. The nanometre-scale physiology of bone: steric modelling and scanning transmission electron microscopy of collagen-mineral structure. Journal of the Royal Society Interface. 2012;9:1774-86.
[15] Jantou-Morris V, Horton MA, McComb DW. The nano-morphological relationships between apatite crystals and collagen fibrils in ivory dentine. Biomaterials. 2010;31:5275-86.

[16] Glimcher MJ. Bone: Nature of the calcium phosphate crystals and cellular, structural, and physical chemical mechanisms in their formation. Rev Mineral Geochem. 2006;64:223-82.
[17] Pan YM, Fleet ME. Compositions of the apatite-group minerals: Substitution mechanisms and controlling factors. Phosphates: Geochemical, Geobiological, and Materials Importance. 2002;48:13-49.
[18] Landis WJ, Song MJ, Leith A, Mcewen L, Mcewen BF. Mineral and Organic Matrix Interaction in Normally Calcifying Tendon Visualized in 3 Dimensions by High-Voltage Electron-Microscopic Tomography and Graphic Image-Reconstruction. Journal of Structural Biology. 1993;110:39-54.
[19] Hodge AJ, Petruska JA. Aspects of protein structure. New York, NY: Academic Press; 1963.
[20] Boonrungsiman S, Gentleman E, Carzaniga R, Evans ND, McComb DW, Porter AE, et al. The role of intracellular calcium phosphate in osteoblast-mediated bone apatite formation. P Natl Acad Sci USA. 2012;109:14170-5.
[21] Srot V, Bussmann B, Salzberger U, Koch CT, van Aken PA. Linking Microstructure and Nanochemistry in Human Dental Tissues. Microscopy and Microanalysis. 2012;18:509-23.
[22] Yonehara K, Shinohara M, Kanaya K. Transmission Electron-Microscopic X-Ray Quantitative-Analysis of Human Dentin at 200 Kv Accelerating Voltage. J Electron Micr Tech. 1990;16:240-8.
[23] Yoshiyama M, Noiri Y, Ozaki K, Uchida A, Ishikawa Y, Ishida H. Transmission Electron-Microscopic Characterization of Hypersensitive Human Radicular Dentin. J Dent Res. 1990;69:1293-7.
[24] Eddisford P, Brown A, Brydson R. Identifying and quantifying the mechanism of electron beam induced damage and recovery in hydroxyapatite. J Phys Conf Ser. 2008;126.
[25] von Harrach HS, Dona P, Freitag B, Soltau H, Niculae A, Rohde M. An integrated Silicon Drift Detector System for FEI Schottky Field Emission Transmission Electron Microscopes. Microscopy and Microanalysis. 2009;15:208-9.
[26] von Harrach HS, Dona P, Freitag B, Soltau H, Niculae A, Rohde M. An Integrated Multiple Silicon Drift Detector System for Transmission Electron Microscopes. Electron Microscopy and Analysis Group Conference 2009 (Emag 2009). 2010;241.
[27] Miller LM, Vairavamurthy V, Chance MR, Mendelsohn R, Paschalis EP, Betts F, et al. In situ analysis of mineral content and crystallinity in bone using infrared micro-spectroscopy of the v(4) PO43- vibration. Bba-Gen Subjects. 2001;1527:11-9.
[28] Young MF. Bone matrix proteins: their function, regulation, and relationship to osteoporosis. Osteoporosis Int. 2003;14:S35-S42.
[29] Martin E, Shapiro J. Osteogenesis imperfecta: Epidemiology and pathophysiology. Curr Osteoporos Rep. 2007;5:91-7.
[30] Lam RSK, Metzler RA, Gilbert P, Beniash E. Anisotropy of Chemical Bonds in Collagen Molecules Studied by X-ray Absorption Near-Edge Structure (XANES) Spectroscopy. Acs Chemical Biology. 2012;7:476-80.
[31] Cosmidis J, Benzerara K, Nassif N, Tyliszczak T, Bourdelle F. Characterization of Ca-phosphate biological materials by scanning transmission X-ray microscopy (STXM) at the Ca L2,3-, P L2,3- and C K-edges. Acta Biomaterialia. 2015;12:260-9.
[32] Pasteris JD, Wopenka B, Valsami-Jones E. Bone and tooth mineralization: Why apatite? Elements. 2008;4:97-104.
[33] Brandes JA, Wirick S, Jacobsen C. Carbon K-edge spectra of carbonate minerals. Journal of Synchrotron Radiation. 2010;17:676-82.
[34] Nicholson PG, Castro FA. Organic photovoltaics: principles and techniques for nanometre scale characterization. Nanotechnology. 2010;21:26.
[35] Etxebarria I, Ajuria J, Pacios R. Solution-processable polymeric solar cells: A review on materials, strategies and cell architectures to overcome 10%. Organic Electronics. 2015;19:34-60.
[36] Green MA, Emery K, Hishikawa Y, Warta W, Dunlop ED. Solar cell efficiency tables (Version 45). Prog Photovoltaics. 2015;23:1-9.

[37] Shaw PE, Ruseckas A, Samuel IDW. Exciton diffusion measurements in poly(3-hexylthiophene). Advanced Materials. 2008;20:3516-+.
[38] Yu G, Gao J, Hummelen JC, Wudl F, Heeger AJ. POLYMER PHOTOVOLTAIC CELLS - ENHANCED EFFICIENCIES VIA A NETWORK OF INTERNAL DONOR-ACCEPTOR HETEROJUNCTIONS. Science. 1995;270:1789-91.
[39] Noriega R, Rivnay J, Vandewal K, Koch FPV, Stingelin N, Smith P, et al. A general relationship between disorder, aggregation and charge transport in conjugated polymers. Nature materials. 2013;12:1038-44.
[40] van Bavel S, Sourty E, de With G, Loos J. Three-dimensional nanoscale organization of bulk heterojunction polymer solar cells. Nano Lett. 2009;9:507-13.
[41] van Bavel S, Sourty E, de With G, Frolic K, Loos J. Relation between Photoactive Layer Thickness, 3D Morphology, and Device Performance in P3HT/PCBM Bulk-Heterojunction Solar Cells. Macromolecules. 2009;42:7396-403.
[42] Drummy LF, Davis RJ, Moore DL, Durstock M, Vaia RA, Hsu JWP. Molecular-Scale and Nanoscale Morphology of P3HT:PCBM Bulk Heterojunctions: Energy-Filtered TEM and Low-Dose HREM. Chem Mater. 2011;23:907-12.
[43] Pfannmoller M, Kowalsky W, Schroder RR. Visualizing physical, electronic, and optical properties of organic photovoltaic cells. Energ Environ Sci. 2013;6:2871-91.
[44] Herzing AA, Richter LJ, Anderson IM. 3D Nanoscale Characterization of Thin-Film Organic Photovoltaic Device Structures via Spectroscopic Contrast in the TEM. Journal of Physical Chemistry C. 2010;114:17501-8.
[45] Pfannmoller M, Flugge H, Benner G, Wacker I, Sommer C, Hanselmann M, et al. Visualizing a Homogeneous Blend in Bulk Heterojunction Polymer Solar Cells by Analytical Electron Microscopy. Nano Lett. 2011;11:3099-107.
[46] Pfannmoller M, Flugge H, Benner G, Wacker I, Kowalsky W, Schroder RR. Visualizing photovoltaic nanostructures with high-resolution analytical electron microscopy reveals material phases in bulk heterojunctions. Synthetic Metals. 2012;161:2526-33.
[47] Gilchrist JB, Basey-Fisher TH, Chang SCE, Scheltens F, McComb DW, Heutz S. Uncovering Buried Structure and Interfaces in Molecular Photovoltaics. Advanced Functional Materials. 2014:n/a-n/a.
[48] Favia P, Voroshazi E, Heremans P, Bender H. Investigation of aged organic solar cell stacks by cross-sectional transmission electron microscopy coupled with elemental analysis. J Mater Sci. 2013;48:2908-19.
[49] Kozub DR, Vakhshouri K, Orme LM, Wang C, Hexemer A, Gomez ED. Polymer Crystallization of Partially Miscible Polythiophene/Fullerene Mixtures Controls Morphology. Macromolecules. 2011;44:5722-6.
[50] Schindler W, Wollgarten M, Fostiropoulos K. Revealing nanoscale phase separation in small-molecule photovoltaic blends by plasmonic contrast in the TEM. Organic Electronics. 2012;13:1100-4.
[51] Herzing AA, Ro HW, Soles CL, Delongchamp DM. Visualization of Phase Evolution in Model Organic Photovoltaic Structures via Energy-Filtered Transmission Electron Microscopy. Acs Nano. 2013;7:7937-44.
[52] Huang Y, Liu XF, Wang C, Rogers JT, Su GM, Chabinyc ML, et al. Structural Characterization of a Composition Tolerant Bulk Heterojunction Blend. Adv Energy Mater. 2014;4.
[53] Gu Y, Wang C, Liu F, Chen JH, Dyck OE, Duscher G, et al. Guided crystallization of P3HT in ternary blend solar cell based on P3HT:PCPDTBT:PCBM. Energ Environ Sci. 2014;7:3782-90.
[54] Guerrero A, Pfannmoller M, Kovalenko A, Ripolles TS, Heidari H, Bals S, et al. Nanoscale mapping by electron energy-loss spectroscopy reveals evolution of organic solar cell contact selectivity. Organic Electronics. 2015;16:227-33.
[55] Mendis BG, Bishop SJ, Groves C, Szablewski M, Berlie A, Halliday DP. Plasmon-loss imaging of polymer-methanofullerene bulk heterojunction solar cells. Applied Physics Letters. 2013;102:4.

[56] Bosman M, Watanabe M, Alexander DTL, Keast VJ. Mapping chemical and bonding information using multivariate analysis of electron energy-loss spectrum images. Ultramicroscopy. 2006;106:1024-32.
[57] Allen FI, Watanabe M, Lee Z, Balsara NP, Minor AM. Chemical mapping of a block copolymer electrolyte by low-loss EFTEM spectrum-imaging and principal component analysis. Ultramicroscopy. 2011;111:239-44.
[58] Yakovlev S, Libera M. Dose-limited spectroscopic imaging of soft materials by low-loss EELS in the scanning transmission electron microscope. Micron. 2008;39:734-40.